Somite morphogenesis is required for axial blood vessel formation

Eric Paulissen[1], Joshua S. Waxman[2], & Benjamin L. Martin[1]*

1 Department of Biochemistry and Cell Biology
Stony Brook University
Stony Brook, NY, USA 11794-5215

2 Molecular Cardiovascular Biology Division and Heart Institute
Cincinnati Children's Hospital Medical Center
Department of Pediatrics, University of Cincinnati College of Medicine,
Cincinnati, OH, USA 45229

*** Correspondence: benjamin.martin@stonybrook.edu**

Summary statement

Retinoic acid induced somite morphogenesis generates a midline cavity that accommodates migrating angioblasts, which form the axial blood vessels.

ABSTRACT

Angioblasts that form the major axial blood vessels of the dorsal aorta and cardinal vein migrate towards the embryonic midline from distant lateral positions. Little is known about what controls the precise timing of angioblast migration and their final destination at the midline. Using zebrafish, we found that midline angioblast migration requires neighboring tissue rearrangements generated by somite morphogenesis. The somitic shape changes cause the adjacent notochord to separate from the underlying endoderm, creating a ventral midline cavity that provides a physical space for the angioblasts to migrate into. The anterior to posterior progression of midline angioblast migration is facilitated by retinoic acid induced anterior to posterior somite maturation and the subsequent progressive opening of the ventral midline cavity. Our work demonstrates a critical role for somite morphogenesis in organizing surrounding tissues to facilitate notochord positioning and angioblast migration, which is ultimately responsible for creating a functional cardiovascular system.

Keywords: Retinoic acid, dorsal aorta, cardinal vein, somite, morphogenesis, ventral midline cavity, notochord endoderm separation, vasculogenesis, angioblasts, mesoderm, zebrafish

INTRODUCTION

Early organismal development relies on a variety of tissues that collectively organize into a functional body plan. In the trunk of the vertebrate embryo, many tissues are differentiating at once, and often interact with one another to influence their definitive structure (McMillen and Holley, 2015). The axial (notochord), paraxial (somites), and lateral (angioblasts and other tissues) mesoderm begins to be specified during gastrulation, and new cells are added to these tissues from posteriorly localized progenitor cells as they expand after gastrulation (Kimelman, 2016; Martin, 2016; Martin and Kimelman, 2012; Row et al., 2016). By the end of embryogenesis, the notochord is a prominent midline tissue of the trunk, and provides structural support to the body and signals that pattern adjacent tissues (Balmer et al., 2016; Glickman et al., 2003; Kimmel et al., 1995). Pairs of somites flank either side of the notochord and give rise to tissues that include the skeletal muscle, tendons, and bone (Tani et al., 2020). Ventral to the notochord and between the somites, the axial vasculature structures of the dorsal aorta and posterior cardinal vein distribute blood throughout the embryo (Hogan and Bautch, 2004; Isogai et al., 2001).

During somitogenesis, newly formed somites undergo a maturation event in which they change their morphology from a cuboidal shape to a chevron shape, and extend in the dorsal-ventral axis (Kimmel et al., 1995; Tlili et al., 2019). Many cellular rearrangements and mechanical stresses contribute to making the final definitive somite shape (Hollway et al., 2007; Leal et al., 2014; Tlili et al., 2019; Yin and Solnica-Krezel, 2007; Yin et al., 2018; Youn and Malacinski, 1981). At the same time that somites are changing shape, endothelial progenitors called angioblasts arise in the lateral plate mesoderm and migrate to the midline of the embryo to form the axial vasculature (Jin et al., 2005). Interestingly, angioblast migration and new somite formation occur in an anterior to posterior progression, with a wave of angioblast migration happening slightly after the wave of somitogenesis (Jin et al., 2005; Kohli et al., 2013; Yabe and Takada, 2016). Despite these two events occurring in close temporal and physical proximity to one another, it is not clear whether they influence each other.

Loss of function mutation of the notochord specifying gene *noto* gene results in non-autonomous migration defects of angioblasts as they move to the midline. (Fouquet et al., 1997; Helker et al., 2015). In the absence of *noto,* the notochord adopts a somitic fate (Fouquet et al., 1997; Talbot et al., 1995). The requirement of notochord specification for angioblast migration suggested that the notochord may act to attract angioblasts to the midline. This model was further explored when a notochord-derived secreted factor named *apela* (also known as *toddler/elabela*) was discovered (Chng et al., 2013; Freyer et al., 2017; Helker et al., 2015; Pauli et al., 2014). This small peptide is expressed in the notochord and when mutated caused angioblast migration defects. However, *apela* loss of function also causes defects in mesoderm and endoderm formation prior to notochord and angioblast specification, via gastrulation defects (Freyer et al., 2017; Norris et al., 2017; Pauli et al., 2014). Similarly, *noto* loss of function causes morphological changes that could interfere with angioblast migration, including a broad expansion of somite tissue near the developing blood vessels (Halpern et al., 1995). Thus, although it appears that mutations that affect notochord development can disrupt angioblast migration, the mechanism of this effect is not clear.

As new somites form during body axis extension, they secrete all-trans retinoic acid (RA). RA is a metabolic derivative of vitamin A, and a series of alcohol and aldehyde dehydrogenases convert Vitamin A into RA in specific locations of the embryo including newly formed somites (Duester, 2008). RA acts as a morphogen with broad roles during vertebrate embryogenesis. Some of these include the development of the limb, skeleton, hindbrain, and heart (Emoto et al., 2005; Heine et al., 1986; Lohnes et al., 1994; Mendelsohn et al., 1994; Niederreither et al., 2001; Sandell et al., 2007). Although involved in many processes, RA has a particular influence over the maturation of mesoderm and somitic tissue (Hamade et al., 2006; Janesick et al., 2018, 2014; Li et al., 2015). While RA is notably involved in ensuring the bilateral symmetry of the somites, it is ultimately dispensable for axis elongation in the zebrafish (Berenguer et al., 2018; Bernheim and Meilhac, 2020; Hamade et al., 2006; Kumar and Duester, 2014). Based on the timing of somite derived RA signaling activity relative to when angioblasts migrate to the midline, we speculated it may be involved in midline angioblast migration.

121 Here we show that RA mediated somite maturation is required for the proper formation
122 of the axial vasculature through a non-autonomous role in inducing morphological
123 changes in surrounding tissues. A process we call notochord-endoderm separation
124 (NES) occurs prior to angioblast migration, wherein the notochord and endoderm
125 separate along the dorsal-ventral axis to generate a cavity we refer to as the ventral
126 midline cavity (VMC). The angioblasts migrate into the VMC after proper NES. The
127 induction of NES and the VMC is somite maturation dependent, and a delay or failure in
128 NES can cause systemic angioblast migration defects. This evidence places somite-
129 maturation as a critical event that is required for NES and the development of the axial
130 vasculature.
131
132 **RESULTS**
133
134 **Retinoic acid promotes convergence of angioblasts to the midline and the**
135 **formation of the vasculature**
136
137 To determine if RA signaling impacts angioblast migration, we made time-lapse movies
138 of *tg(kdrl:GFP)* embryos, which express GFP in angioblasts (Jin et al., 2005). Embryos
139 were mounted at the 10 somite-stage and their migration was observed over a 3-hour
140 time period. Wild type angioblasts migrated to the midline in a manner consistent with
141 previously described research (Figure 1A, Supplemental Movie 1) (Helker et al., 2015;
142 Jin et al., 2005; Kohli et al., 2013). To determine what effect the loss of RA would have
143 on the migrating angioblasts, we generated *aldh1a2* mutants with the *tg(kdrl:GFP)*
144 transgenic angioblast reporter in the background. Time-lapse imaging of these embryos
145 shows defects in angioblast migration to the midline (Figure 1B, Supplemental Movie 2),
146 which was also confirmed by in-situ hybridization (Figure S1). Three other methods of
147 disrupting RA signaling caused the same phenotype. Loss of RA by treatment with N,N-
148 diethylaminobenzaldehyde (DEAB) (an inhibitor of the Aldh family, including Aldh1a2
149 (Morgan et al., 2015)), the small molecule retinoic acid receptor (RAR) alpha and
150 gamma inhibitor (BMS453), or expression of a dominant negative RARa using the
151 *Tg(hsp70l:EGFP-dnHsa.RARA)* transgenic line (hereafter referred to as *HS:dnRAR)* all
152 caused midline migration defects (Skvarca et al., 2019) (Figure S1). Angioblasts in these
153 embryos show no clear anterior to posterior migration patterns and are often
154 disorganized in their directionality. Conversely, we also sought to determine if addition of

RA accelerated angioblast migration. We compared the angioblast migration patterns of 10 somite stage *tg(kdrl:GFP)* embryos treated with either DMSO (vehicle) or 0.1 μM RA at the tailbud stage (Figure 1C,1D, respectively). Angioblasts in the DMSO treated embryos migrate normally, but the angioblasts treated with RA reached the midline earlier in development (Figure 1C and Figure 1D, respectively, Supplemental Movie 3). To determine the rate at which angioblasts reach the midline, we quantified the percentage of GFP fluorescence at the midline in relation to the total amount of fluorescence for the both wild type, *aldh1a2* -/-, and 0.1 μM RA embryos. We defined angioblast fluorescence as reaching the midline if they are settled beneath the notochord. The *aldh1a2* -/- embryos show very low percentage fluorescence at the midline, relative to total fluorescence, compared to wild type embryos 4 hours after observation, when angioblast migration is largely complete (Figure 1E). However, fluorescence was higher at the midline in embryos treated with RA than in DMSO treated embryos (Figure 1E). This shows that RA is necessary and sufficient for promoting angioblast migration to the midline. To determine at which stage RA is needed for angioblasts to migrate to the midline, we administered DEAB at different stages of development. Inhibition of RA at tailbud stage caused the angioblast migration defect, but treatment at the 5 somite stage resulted in normal migration (Figure 1G and 1H, respectively).

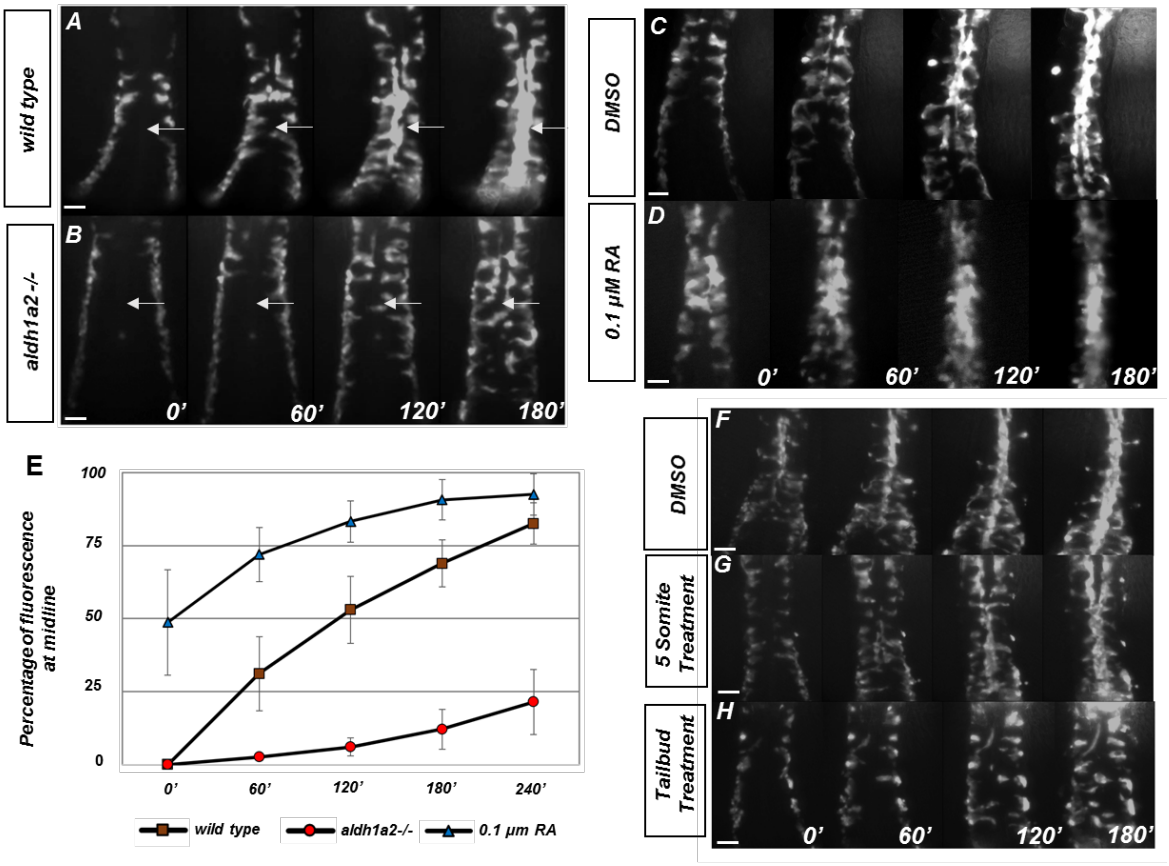

174

Figure 1.Retinoic acid is required prior to segmentation for angioblast migration. (**A**) Dorsal view of a *tg(kdrl:eGFP)* embryo with representative images taken every 60 minutes over the course of 180 minutes, with the anterior of the embryo at the top. White arrows indicate the midline (n=12) (see Supplemental Movie 1). (**B**) Images of *tg(kdrl:eGFP), aldh1a2* -/- embryos taken every 60 minutes over the course of 180 minutes (n=12) (see Supplemental Movie 2). (**C**) *tg(kdrl:eGFP)* embryos treated with DMSO (n=10). (**D**) *tg(kdrl:eGFP)* embryos treated with 0.1 μM RA (n=8) (see Supplemental Movie 3). (**E**) Graph of corrected fluorescence intensity as it arrives to the midline for wild type, *aldh1a2* -/-, and 0.1 μM RA embryos. Y-axis indicates percentage of fluorescent intensity at midline relative to the fluorescence intensity of whole embryo (n=8 for all conditions). Time is measured on the X-axis. Error bars indicate standard deviation. (**F-H**) *tg(kdrl:eGFP)* embryo time-lapse images treated with either DMSO vehicle (**F**) (n=10), 20 μM DEAB treatment at the 5 somite stage (**G**) (n=6), and 20 μM DEAB at tailbud stage (**H**) (n=14). Scale bars, 50 μm.

175 RA depletion by pharmacological inhibition had previously shown to effect the zebrafish
176 vasculature, notably causing a smaller than normal dorsal aorta (Pillay et al., 2016). To
177 confirm this effect in the *aldh1a2* -/- mutant, we imaged the trunk of 5 dpf *tg(kdrl:GFP)*
178 embryos along with *tg(kdrl:GFP), aldh1a2* -/- siblings (Figure 2A,2B). The *tg(kdrl:GFP)*
179 embryos alone showed no vascular defects and normal dorsal aorta and posterior
180 cardinal vein (Figure 2A, white arrow and yellow arrowhead respectively). However, the

vasculature of the *aldh1a2* -/- siblings show a large reduction of the size of the dorsal aorta (Figure 2B, white arrow). In addition, it appears that the posterior cardinal vein of *aldh1a2* -/-increased in size compared to its sibling (Figure 2B, gold arrowhead). Since it is possible that the apparent reduced size of the DA could be the result of a collapsed structure, we examined if the DA was properly lumenized in the embryo. We sectioned 24 hpf *tg(kdrl:GFP)* and *aldh1a2* -/- embryos, stained the sections with DAPI, and imaged them using spinning disk confocal microscopy (Figure 2C,2D). Images show that the dorsal aorta and posterior cardinal vein in wild type embryos are roughly equivalent in size (Figure 2C, white arrows). However, in the *aldh1a2* -/-, the size of the dorsal aorta is reduced but remained lumenized (Figure 2D, white arrows). In-situ hybridization of the arterial marker *cldn5b* and the venous marker *dab2* shows similar effects (Figure S2A-D) (Casie Chetty et al., 2017). To determine if the size change was the result of a reduced cell number in the DA in response to RA loss, we utilized the transgenic line *tg(kdrl:nls-GFP)*, which labels the nucleus of endothelial cells to count the number of cells in each blood vessel over a 225 μM horizontal section of a 24 hpf zebrafish embryo. Embryos were treated with either DMSO, or with DEAB to inhibit RA. We see reduced cell number in the DEAB treated artery versus the DMSO treated artery (Figure 2E). This corresponds to an increase number of cells in the veins during DEAB treatment compared to DMSO. This indicates that more endothelial cells sorted into the vein.

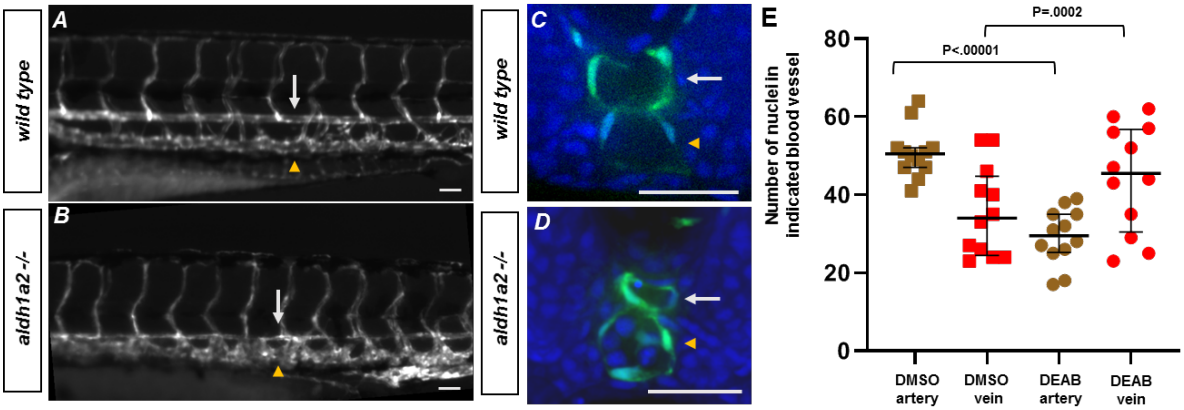

Figure 2. Retinoic acid loss causes changes in the definitive vasculature resulting in large veins and small arteries.
(**A**) A 5 dpf *tg(kdrl:eGFP)* embryo. White arrows indicate the dorsal aorta and yellow arrowheads indicate the cardinal vein. (**B**) 5 dpf *tg(kdrl:eGFP), aldh1a2-/-* embryo. White arrows indicate reduced size of dorsal aorta. (**C-D**) 25 hpf *tg(kdrl:eGFP).* embryo labeled with DAPI . (**C**) Wild type embryos show lumenized blood vessels and normal sized dorsal aorta. (**D**) Labeled *aldh1a2 -/-, tg(kdrl:eGFP)* sibling shows small lumenized dorsal aorta with large posterior cardinal vein. (**E**) Quantification of DMSO (n=12) or 20 μM DEAB (n=12) treated *tg(kdrl:nls-eGFP)* embryos. Nuclei were counted in each structure over a 225 μM long transverse section of the zebrafish trunk. Two-tailed *P*-values for the unpaired t-test of wild type vs 20 μM DEAB treated embryos are <.00001 and .0002 for arteries and veins, respectively. Scale bars, 50 μm.

Retinoic acid is required cell non-autonomously for angioblast migration.

To determine if RA functions cell autonomously to induce angioblast migration, we utilized the transgenic zebrafish line *Tg(hsp70l:id3-2A-NLS-KikGR),* which carries a heat shock inducible construct that overexpresses *id3* after a temperature shift (Row et al., 2018). We previously showed that overexpression of *id3* from this line can cause transplanted cells from a donor embryo to faithfully adopt an endothelial fate in a wild-type host embryo. (Row et al., 2018). We utilized this by crossing *Tg(hsp70l:id3-2A-NLS-KikGR))*, hereafter referred to *HS:id3*, to *HS:dnRAR,* to generate donor embryos wherein transplanted cells would be targeted to the endothelium and express dominant negative retinoic acid receptors (RARA). Cells positive for both transgenic constructs were transplanted into *tg(kdrl:eGFP)* host embryos and exhibited normal migration to the midline (Figure 3A, Supplemental Movie 4). In addition, we utilized a RA reporter line, *tg(RDBD,5XUAS:GFP),* to determine which tissues were subject to RA signaling (Mandal et al., 2013). We performed immunohistochemistry against GFP and the transcription factor Etv2, which labels the angioblasts (Figure 3B) (Sumanas et al., 2005). GFP expression indicates tissues that have been exposed to RA. Tissues that received RA, which include the adaxial region of the somites, notochord, and epidermis (Figure 3B, white arrow, white arrowhead, and gold arrow, respectively). The primitive angioblasts, labeled with anti-Etv2 staining, do not overlap with GFP staining (Figure 3B, red arrows). Together these results indicate that angioblasts are not receiving an RA signal and do not require RA signaling for migration when surrounded by a wild-type

environment.

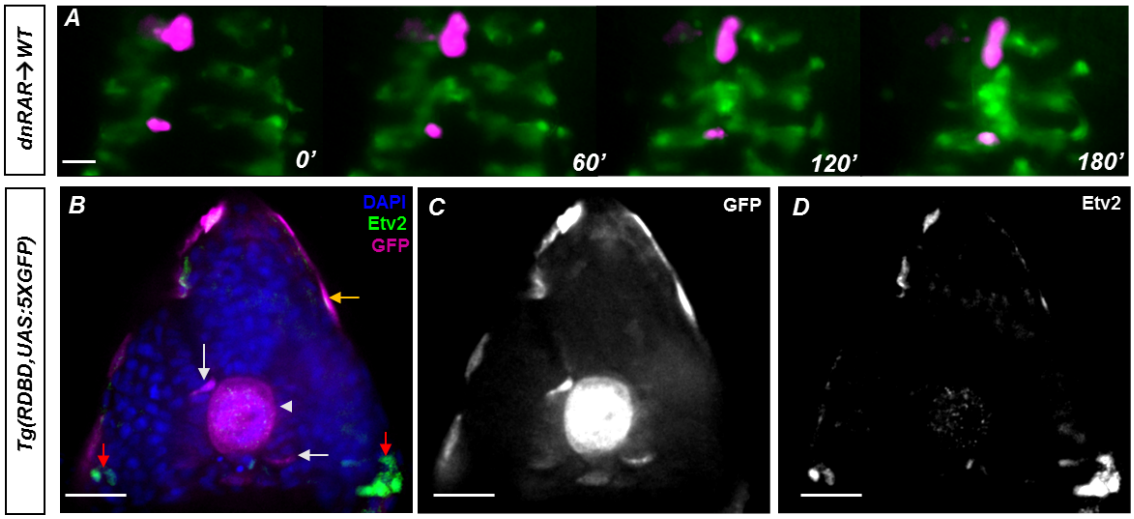

Retinoic acid is required to induce notochord-endoderm separation and generate the ventral midline cavity.

Since RA signaling is required non-autonomously for angioblast migration, we investigated whether inhibition of RA signaling disrupted the neighboring somites or notochord in a manner which could account for angioblast migration defects.. We crossed the *tg(actc1b:gfp)* and *tg(tbxta:kaede)* transgenic lines to label the somites and

Figure 3. Retinoic acid signaling is not present in the endothelium and is required cell non-autonomously for angioblast migration.
(**A**) Representative images of a time-lapse of *tg(HS:dnRAR)*, *tg(HS:id3)* cells transplanted into a wild type embryo. Cells labeled in magenta indicate migrating cells. These cells migrate along with the host angioblasts labeled by *tg(kdrl:gfp),* indicating normal migration patterns in absence of cell-autonomous RA depletion conditions (n=3) (see Supplemental Movie 4). (**B**) DAPI stained section of 13-somite-stage *tg(RDBD,5XUAS:GFP)* embryo, immunostained for GFP and Etv2 (n=12). GFP signal is present in adaxial region of the somite, the notochord, and the epidermis (white arrow, white arrowhead, and gold arrows, respectively). The red arrows indicate areas of Etv2 staining. (**C**) GFP channel of image in (B). (**D**) Etv2 channel of image in (B). Note the lack of overlap between Etv2 staining and GFP staining. Scale bars, 50 µm.

notochord, respectively. Transgenic reporter embryos were treated with either DMSO or DEAB and time-lapse imaged beginning at the 10-somite stage for 250'. In both DMSO and DEAB treated embryos, the notochord begins immediately adjacent to the

239 endoderm (Figure 4A, 4C). After 4 hours of observation in DMSO treatmed embryos, the
240 notochord displaces dorsally relative to the underlying endoderm (Figure 4B,
241 Supplemental Movie 5). However, the notochord of *DEAB* treated embryos showed no
242 signs of displacement (Figure 4D, Supplemental Movie 6). Treatment with exogenous
243 RA had the opposite effect, with embryos showing premature displacement of the
244 notochord away from the endoderm (Figure 4E and 4F, Supplemental Movie 7).
245 Quantification of movements from the 10-somite stage embryos, over a 250' period,
246 confirms these observations. The *aldh1a2 -/-* mutant embryos did not have significant
247 dorsal movement of the notochord until 250', while wild-type embryos showed significant
248 dorsal movement at 150' (Figure 4G, red circles and brown squares, respectively).
249 Embryos treated with exogenous RA showed significant dorsal movement even at the
250 10-somite stage (Figure 4G, blue triangles). In order to better analyze the tissues at the
251 midline, we utilized *tg(hsp70l:CAAX-mCherry-2A-NLS-KikGR),* hereafter referred to as
252 *HS:mcherry-caax,* to label cellular membranes in red, and sectioned embryos at
253 approximately the third somite. Sections of DMSO and DEAB treated embryos at the 10-
254 somite stage showed identical positioning of the notochord (Figure 4H, 4K). However, at
255 the 13 and 15-somite-stage, the notochord in DMSO treated embryos moved dorsally,
256 while the notochord in DEAB treated embryos did not (Figure 4I,4J and Figure 4L,4M
257 respectively, white arrows). We termed this dorsal movement of the notochord away
258 from the endoderm the notochord-endoderm separation (NES).
259

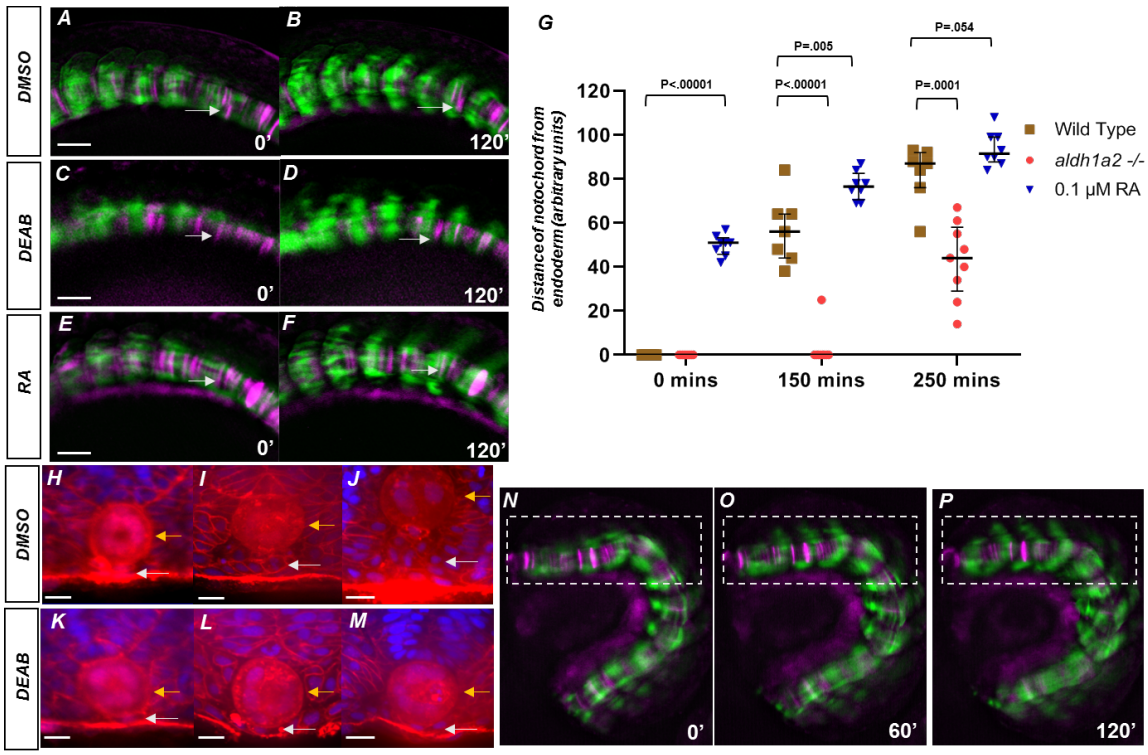

Figure 4: Sections of labeled embryos show an notochord-endoderm separation that is retinoic acid dependent and the zebrafish trunk is sufficient for NES. (**A-F**) Fluorescent images of *tg(tbxta:kaede), tg(actc1b:gfp)* embryos labeling the notochord and somites, respectively. (**A,C,E**) 10-somite stage embryos at time 0' (**B,D, F**) Embryos after 120' of development. (**A-B**) *DMSO* (n=6) (**C-D**) 20 μM DEAB (n=7) (**E-F**) 0.1 μM RA (n=8). White arrows indicate position of ventral notochord. (**G***)* Quantification of notochord lifting from the ventral tissue. Black lines indicate the median and interquartile range. Wild type are indicated by brown squares, while *aldh1a2 -/-* and 0.1 μM RA embryos are shown by red circles and blue triangles, respectively. At t=0, DMSO vs. RA is P<.00001. At 150', DMSO is P<.00001 and P=.005 vs. *aldh1a2 -/-* and RA treatment, respectively. At 250', DMSO is P=.0001 and .054 vs. *aldh1a2 -/-* and RA treatment, respectively. (**H-M**) Fixed *HS:mcherry-caax* embryo sections labeled with DAPI. (**H-J**) DMSO treatment. (**K-M**) 20 μM DEAB treatment. (**H,K**) 10-somite stage (**I,L**) 13-somite stage (**J,M**) 15-somite stage. White arrows indicates tissue ventral to notochord. Yellow arrows indicate the notochord. *Wild type* embryos show a change in notochord position relative the ventral embryo while DEAB treatment show little change. (**N-P**) Time-lapse image of a trunk explant from *tg(actc1b:gfp), tg(tbxta:kaede)* embryo. (**N**) 0'. (**0**) 60' (**P**) 120'. Time-lapse shows the notochord adjacent the yolk at time 0', but moved dorsally from the yolk at time 120'. Scale bars, 25 μm.

Previous work showed that as somites mature, they extend in the both the dorsal and ventral axis (Tlili et al., 2019), and based on this we hypothesized that that somite morphogenesis is responsible for causing NES. However, we wanted to rule out the effect of forces on the anterior-most and posterior-most regions of the notochord. The

266 notochord is a rigid structure that is anchored in the tailbud near the notochord
267 primordia, and extends into the head mesoderm medial to the otic vesicle (Kimmel et al.,
268 1995). To eliminate the contribution other tissues could have on NES, we generated
269 trunk explants from *tg(actc1b:gfp)* and *tg(tbxta:kaede)* embryos that contained roughly
270 10 somites of the embryo. The 10 somite stage embryos were sectioned near the somite
271 borders of the 1st and 10th somite. Live imaging of these trunk explants showed that
272 immature somites in the posterior were able to adopt a mature chevron shape (Figure
273 4N-4P, Supplemental Movie 8). In addition, the notochord was able to separate from the
274 endoderm during this process. This data indicates the zebrafish trunk is sufficient for
275 NES, and the tissues contributing to NES are restricted to that region.
276
277 Given that RA signaling promotes NES, we wanted to determine if midline migration of
278 angioblasts were correlated with NES. We crossed *tg(kdrl:GFP)* to *HS:mcherry-caax*
279 embryos and induced *mcherry-caax* at shield stage. We then fixed embryos at the 13
280 somite stage and stained the embryos with DAPI prior to sectioning. For drug
281 treatments, the embryos were treated with either DMSO or 20 μM DEAB at the tailbud
282 stage. In DMSO treated embryos, angioblasts migrate between the notochord and the
283 endoderm and occupy the space created by NES (Figure 5A, 5B, white arrows). This
284 space we have termed the Ventral Midline Cavity (VMC). In DEAB treated embryos,
285 angioblasts are located at the lateral edges of the embryo (Figure 5C, 5D, white arrows).
286 The notochord is pressed to the endoderm in this condition, and lack a VMC (Figure 5D,
287 gold arrow). To better observe angioblast migration to the midline, we used a live explant
288 method to monitor migrating from a transverse section view. Live *tg(kdrl:GFP)* embryos
289 were sectioned at the 10-somite stage at the 4th somite and mounted to observe a
290 transverse section of the trunk. We were able to observe angioblasts migrating to the
291 ventral midline in the context of embryological movement in a wild type embryo (Figure
292 5E, Supplemental Movie 9). Observation of the same phenomena in *tg(kdrl:GFP),*
293 *aldh1a2* -/- embryos showed angioblasts at lateral positions that failed to cross into the
294 midline, accompanied by very little notochord movement (Figure 5F, Supplemental
295 Movie 10).

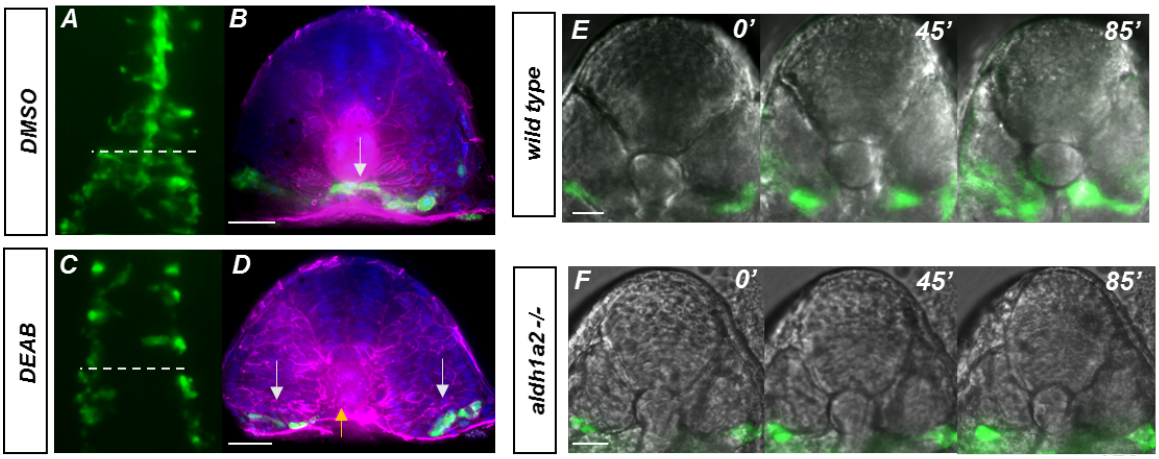

Figure 5. Migrating angioblasts enter into the emerging ventral midline cavity as NES progresses.
(**A**) Fluorescent images of migrating *tg(kdrl:GFP)* angioblasts. *tg(kdrl:GFP)* angioblasts where white line indicates approximate sectioning area. (**B**) Section of *tg(kdrl:GFP) (green),(HS:mcherry-caax) (magenta)* embryo stained with DAPI *(blue)* (n=12). (**C**) *tg(kdrl:GFP)* angioblasts in DEAB treated embryo, where white line indicates rough sectioning area. (**D**) Section of a *tg(kdrl:GFP),(HS:mcherry-caax)* embryo treated with 20 μM DEAB (n=12). (**E**) Live image of *tg(kdrl:GFP)* explant over 85 minute period. Angioblasts are labeled in green with DIC in grey. (n=7) (**F**) Live image of *tg(kdrl:GFP), aldh1a2 -/-* explant over 85 minute period (n=6). Scale bars, 50 μm.

The somitic mesoderm is required for angioblast migration to the midline.

We next determined whether the notochord itself was required for VMC formation. Previous studies have investigated genes linking the notochord to angioblast migration. Mutants of the genes *noto* and *apela* were found to be notochord specific genes required for proper angioblast migration (Cleaver and Krieg, 1998; Fouquet et al., 1997; Helker et al., 2015). The *noto* gene induces notochord, and the notochord in turn secretes Apela which attracts the angioblasts to the midline. However, there are also broad morphological changes in these mutants that could contribute to the migration defect. We decided to determine if these previously identified genes were associated with similar defects to what is seen in RA signaling loss of function. Noto is required for the formation of the notochord, and in the absence of Noto, the midline cells adopt a somitic fate (Talbot et al., 1995). We injected a *noto* morpholino that faithfully phenocopies the *noto* mutant into *tg(kdrl:GFP)* embryos (Ouyang et al., 2009). Control morphant embryos show normal angioblast migration (Figure 6A), whereas *noto* morphants show slowed

313 angioblast migration (Figure 6B). However, midline convergence still occurs in both
314 conditions, albeit with unorganized structure in the *noto* morphants (Figure 6C and
315 Figure 6D, respectively). This implies that the notochord is ultimately dispensable for the
316 formation of the VMC and midline positioning of angioblasts.
317
318 Having ruled out the role of notochord tissue, we next investigated whether the somitic
319 mesoderm is required for NES and the formation of the VMC. Previous studies have
320 shown that the t-box transcription factor *tbx16* is required for proper somite formation
321 (Amacher et al., 2002; Goto et al., 2017; Griffin et al., 1998; Kimmel et al., 1989;
322 Manning and Kimelman, 2015; Row et al., 2011). In the absence of tbx16, cells that
323 would normally join the paraxial mesoderm fail to do so, causing a deficiency in the trunk
324 somitic mesoderm. We utilized *tbx16* mutants to determine whether the lack of somites
325 caused angioblast migration defects, similar to RA loss of function. We examined midline
326 angioblast migration in *tbx16* mutant embryos with the *tg(kdrl:GFP)* transgene in the
327 background. In wild type sibling embryos, angioblast migration progresses normally to
328 the midline (Figure 6E). However, in *tbx16* -/- embryos, angioblast migration does not
329 occur, as they remain in their positions in the lateral plate (Figure 6F). Transverse
330 sections of *tg(kdrl:GFP)* embryos injected with *tbx16* morpholinos that phenocopy the
331 mutant show that NES does not occur and the VMC is absent, and that angioblasts
332 adopt two blood vessel structures on either side of the notochord (Figure 6G).
333 Interestingly, these bifurcated angioblasts preferentially adopt a venous fate over the
334 arterial fate (Figure S3B-S3D). This indicates that the somitic mesoderm is required for
335 NES and formation of the VMC, which in turn is necessary for the angioblasts to reach
336 the midline.

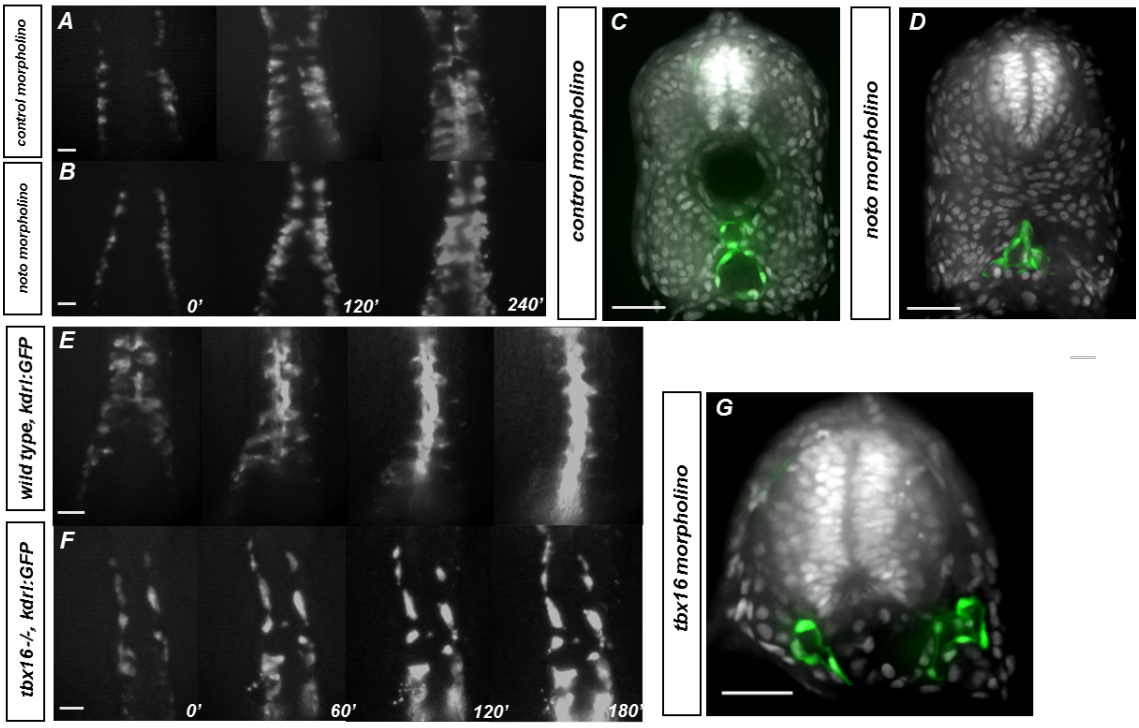

Figure 6. Genes which affect angioblast migration also effect somitic mesoderm and ventral cavity formation.
(**A**) Time-lapse imaging of *tg(kdrl:eGFP)* embryos injected with control morpholino over a 240' period. (**B**) *tg(kdrl:eGFP)* embryos injected with *noto* morpholino over a 240' period. (**C**) Section of 24 hpf *tg(kdrl:eGFP)* embryos injected control morpholino and stained with DAPI. Blood vessels are labeled in green and nuclei labeled in grey. (**D**) Section of 24 hpf *tg(kdrl:eGFP)* embryos injected *noto* morpholino and stained with DAPI. (**E**) Timelapse imaging of wild type, *tg(kdrl:eGFP)* embryos over a 240' period. (**F**) Timelapse imaging of *tbx16* -/-, *tg(kdrl:eGFP)* embryos over a 240' period (**G**) Section of 24 hpf *tg(kdrl:eGFP)* embryos injected *tbx16* morpholino. Blood vessels are labeled in green and nuclei labeled in grey. Scale bars, 50 µm.

Retinoic acid induced somite morphogenesis facilitates ventral midline cavity formation.

Given the importance of somites for midline angioblast migration, we investigated whether RA is required for somite shape changes that could drive NES. Mosaically labeled cells were generated by transplanting rhodamine dextran labeled cells from a wild type donor into a wild type host. The embryos were treated with either DMSO or DEAB and time-lapse imaged over the course of 4 hours (Figure 7A and Figure 7B, respectively). Cells in DMSO treated embryos showed broad movements consistent with that of somite rotation, where cells located in the anterior of the somite will translocate to

349 the posterior of the somite (Hollway et al., 2007) (Figure 7A, white arrows). However,
350 cells in DEAB treated embryos show little intratissue displacement and cells largely
351 remained static (Figure 7B, white arrows). To quantify this, we utilized *HS:mcherry-caax*
352 embryos to observe cell movement across the entirety of the somite. Embryos were heat
353 shocked during shield stage and subsequently treated with either DMSO or DEAB and
354 their somites were time-lapse imaged for 4 hours. Using Fiji Trackmate software
355 (Tinevez et al., 2017), we quantified the displacement and speed of cell movements
356 within the 2nd somite (Figure 7C and 7D). Cells in DMSO treated embryos showed
357 significant amounts of displacement throughout the somite (Figure 7C). However the
358 DEAB cells showed less displacement over time (Figure 7C). Quantification of speed in
359 the same manner showed no statistically significant difference between DMSO and
360 DEAB treatment (Figure 7D). A sample of somite cell tracks shows little directional
361 movement in loss of RA conditions compared to DMSO, indicating cells are not moving
362 in a manner consistent with reshaping of the somite, as well as suggesting a role for RA
363 signaling in somite rotation (Figure 7E and 7F, Supplemental Movie 11 and 12,
364 respectively). The Cxcr4a/Cxcl12a signaling axis has been shown to be responsible for
365 controlling cell movements in the somite. In-situ hybridization for *cxcr4a* shows a loss of
366 expression in RA depletion conditions and gain of expression in RA addition conditions
367 (Hollway et al., 2007) (Figure S4D and S4E).
368
369 We speculated that the ventral expansion of the somite that occurs during somite cell
370 rearrangement and maturation was responsible for NES. At the 10 somite stage,
371 embryos have their notochord adjacent to the endoderm and level to ventral-most edge
372 of the somite (Figure 7G). As the embryo develops, the somite expands ventrally (black
373 bracket). As the ventral distance of the somite extends relative to the dorsal part of the
374 notochord (yellow bracket), it induces space that the angioblasts occupy (blue brackets).
375 Starting from the 10 somite stage, we measured the distance of ventral expansion
376 relative to the distance between the notochord and the endoderm. We did this every
377 hour for 4 hours. A simple linear regression n of the data, indicated by the black line,
378 shows a slope of 0.002 and y-intercept of 1.04 (Figure 7H). The flat slope indicates little
379 variance across time, and the y-intercept near 1 indicates that NES is roughly equivalent
380 to ventral expansion of the somite. The strong 1:1 correlation of ventral somite
381 expansion and notochord displacement, as well as the *tbx16* loss of function NES
382 defect, provides strong evidence that somite morphogenesis is critical for NES. Sections

of DMSO treated embryos at the 12-somite stage showed a modest NES while DEAB treated embryos showed none (Figure 7I and Figure 7J Gold Arrows). Conversely, embryos treated with exogenous RA showed a more robust NES (Figure 7K. Gold Arrow). In addition to these observations, we observed an apparent somite shape change. Somites extended more in the dorsal-ventral axis in DMSO and RA treated embryos, while DEAB treated embryos adopt a broader medio-lateral shape consistent with immature somites (Figure 7I, Figure 7K, and Figure 7J, respectively. White Arrows).

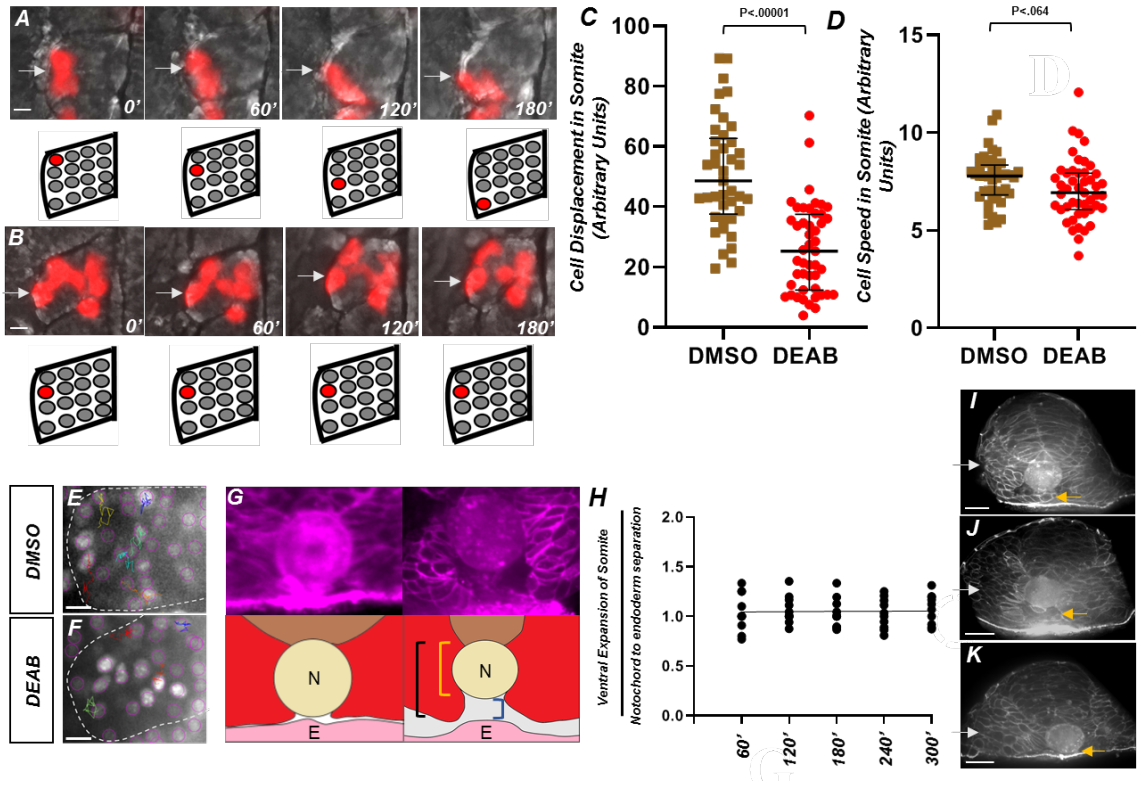

Figure 7. Retinoic acid controls intrasomitic cellular movements, somite shape, and NES.
Time-lapse images of transplanted rhodamine-dextran labeled cells in DMSO and DEAB embryos at 12 somite stage. (**A**) DMSO treated embryos over 180'. White arrows indicate labeled cells (**B**) 20 μM DEAB treated embryos over 180'. Scale bars, 50 μm. Retinoic acid depleted embryos show little cellular movement during somite development. (**C**) Quantification of nuclei displacement in the 2nd somite of DMSO and DEAB embryos over a 4 hour time period. Displacement is defined as the distance between the beginning location and end location of the nuclei within the somite 2. (**D**) Quantification of speed in somite 2, defined as average units over 4 hours in 10 minute increments. (**E**) Sample of tracks of DMSO embryos. (**F**) Sample tracks of DEAB embryos. Tracks sort from red to blue, with red being the highest displacement. Scale bars, 20 μm (**G**) Diagram of ventral somite expansion and notochord to endoderm separation. Ventral somite expansion is calculated by ventral somite length (black bracket) – the notochord diameter (Yellow Bracket). Notochord/endoderm separation is shown in the blue bracket. (**H**) Quantification of the ventral expansion of the somite over notochord/endoderm separation in wild type embryos. The linear regression indicated by the black line, where slope = 0.002, shows ventral somite expansion correlates with notochord/endoderm separation. (**I-K**) *(HS:mcherry-caax)* embryos in RA depletion or exogenous treatment, with RFP in grey. Somites and NES are indicated by white and yellow arrows, respectively. (**I**) DMSO. (**J**) 20 μM DEAB. (**K**) 0.1 μM RA. RA inhibition reduces NES and somite expansion (**I**), while exogenous RA increases NES and somite expansion (**J**) Scale bars, 50 μm.

DISCUSSION

Here, we established a cell nonautonomous angioblast migration model where shape changes in the somitic mesoderm create a physical space to open for the axial vasculature to occupy, via a process we named NES. The emergence of the VMC is a necessary requirement for endothelial progenitors to both migrate into and develop into functioning blood vessels. We observed a defect in somitic mesoderm development when RA signaling is inhibited, which delayed somite maturation, intrasomite cellular movement, and prevented NES. Conversely, we found that addition of RA accelerated somite maturation and NES, and subsequently angioblast migration. We were able to confirm that the somitic mesoderm was required for angioblast migration by examining *tbx16* mutants, which have a lack of somites caused by EMT defects (Goto et al., 2017; Ho and Kane, 1990; Manning and Kimelman, 2015; Row et al., 2011). Loss of function of *tbx16* prevented angioblast migration completely and resulted in bifurcated blood vessel formation. These changes in vascular morphology indicate that the somitic mesoderm is a requirement for angioblast migration to the midline. It is notable that in amniotes, such

408 as the mouse and quail, the dorsal aorta and cardinal vein are initially bifurcated in a
409 similar manner to zebrafish *tbx16* mutants prior to fusion at the midline (Drake and
410 Fleming, 2000; Pardanaud et al., 1996, 1987). It is possible that evolutionary differences
411 in the somitic mesoderm between teleosts and amniotes could play a role in the
412 differences in vascular development.
413
414 Very little is known about the process of NES. Our observations indicate that its initiation
415 correlates very closely with angioblast migration, with angioblasts migrating into the
416 VMC seemingly as soon as it opens. Given that these blood vessels become lumenized,
417 and need to achieve a sufficient volume for blood transport, they require morphological
418 changes within the ventral part of the embryo to accommodate for their size. Delays in
419 somite maturation prevent angioblasts from reaching the midline in a normal
420 developmental time frame. The consequences of this migration defect results in a
421 malformed blood vessel structure with small arteries and larger veins. Prior work showed
422 that the most lateral angioblasts, which migrate later than more medial angioblasts,
423 preferentially adopt a venous fate over an arterial one (Kohli et al., 2013). This implies
424 that somite maturation is a key factor in determining the proper distribution of endothelial
425 progenitors to the arteries and veins, respectively.
426
427 We found that the formation of the VMC does not necessarily require the notochord
428 tissue itself. In *noto* morphants, which causes the notochord to adopt a somitic fate,
429 there is still a ventral cavity and angioblasts are able to arrive at the midline. This implies
430 that the notochord is ultimately dispensable for angioblast migration and NES, even
431 though its loss can produce transient migration defects (Helker et al., 2015; Sumoy et
432 al., 1997). It is possible that signals from the notochord, such as Hedgehog, influence
433 somite development which in turn facilitates angioblast migration (Blagden et al., 1997;
434 Hinits et al., 2009; Yin et al., 2018). While the fate of the midline tissue does not need to
435 be notochord for NES to occur and form the VMC, it is likely that mechanical coupling
436 between the somites and midline tissue is required such that somite morphogenesis
437 drives the separation of the midline mesoderm away from the underlying endoderm. In
438 *noto* loss of function, the somitic tissue that forms at the midline in place of notochord is
439 continuous with the flanking somites. In wild-type embryos, there is evidence of
440 mechanical interactions of the somite and notochord during convergent extension, which

441 are required for the remodeling of the adaxial cells, the medial most cells in the somite
442 (Yin and Solnica-Krezel, 2007).
443
444 The phenotypes observed in both the somites and endothelium after loss of RA signaling
445 are not the result of a simple deficit of mesoderm. RA signaling loss of function affects
446 somite maturation and morphogenesis, but does not prevent them from forming, and yet
447 the migration of the angioblasts is still disrupted. The direct transcriptional targets of RA
448 signaling that induce somite maturation are unknown, but it is clear that RA signaling
449 controls the timing and progress of somite shape changes as they mature. The temporal
450 coupling of angioblast migration and somite shape change appears to be relevant to the
451 overall morphology of the endothelium. While RA depleted embryos do form blood
452 vessels, the reduced size of the dorsal aorta and enlargement of the posterior cardinal
453 vein appear to be a consequence of the somite morphology change. It is possible that
454 the somite itself could facilitate the angioblasts movement to the midline, or simply
455 provide an opening through which angioblasts can reach the midline. However, the fact
456 that angioblasts reside adjacent to the notochord in *tbx16* mutants implies angioblasts
457 will migrate until they are obstructed. Additionally, *noto* morphants have additional
458 somitic mesoderm and still have angioblast migration defects. Together, this indicates
459 that somitic maturation requires tight spatial and temporal control to facilitate the
460 concomitant development of the endothelium.
461
462 **Materials and Methods**
463
464 **In-situ hybridization and immunohistochemistry**
465 Whole-mount in situ hybridization was performed as previously described (Griffin et al.,
466 1995). An antisense RNA probe was synthesized as previously described for *etv2*
467 (Sumanas et al., 2005). The *cldn5b, cxcr4a, and cxcl12a* and *dab2* DIG probes were
468 generated by *taq* polymerase-generated PCR fragments integrated into a pCRII vector
469 using the Topo-TA Cloning kit (Thermo Fisher). Immunohistochemistry was performed
470 by fixing embryos overnight in 4% Paraformaldehyde (Sigma) dissolved in phosphate
471 buffered saline containing 0.1% Tween-20 (PBST) at 4°C. Permeabilization was
472 performed by the placing the embryos in PBS containing 2% Triton X-100 (Sigma) for 1
473 hour with agitation. Embryos were washed 3x with PBST and blocked in a blocking
474 solution (PBST, 10% goat serum, 1% BSA) for 2 hours at room temperature. Primary

475 antibodies, Etv2 Rabbit Polyclonal and GFP mouse monoclonal, were diluted to 1:500 in
476 blocking solution and incubated overnight at 4°C. Embryos were washed 5x with PBST
477 for 20 mins each wash. Embryos were then incubated in blocking solution for 2 hours;
478 and then incubated in the secondary antibodies Alexa Fluor 488 and Alexa Fluor 568
479 diluted 1:1000 in blocking solution at 4°C overnight. DAPI stains were done in a 10
480 µg/mL dilution in PBST for at least 1 hour with agitation.
481
482 **Histological analysis**
483 Sections were fixed overnight in 4% Paraformaldehyde (Sigma) dissolved in phosphate
484 buffered saline containing 0.1% Tween-20 (PBST) at 4°C. Nuclei labeling was done for
485 whole embryos in a 10 µg/mL dilution of DAPI in PBST for at least 1 hour with agitation.
486 Sections, after fixation and DAPI staining, were done in PBST with a 0.15mm microknife
487 (Fine Science Tools), at approximately the 3rd somite for embryos up to 24 hpf. At 24
488 hpf or older, embryos were sectioned at approximately the 7th somite. Sections were
489 mounted in 1% Agarose in PBS in a in a 35mm glass bottom dish with uncoated #1.5
490 coverslip and 20mm glass diameter (MatTek).
491
492 **Microinjections**
493 A mix of two *tbx16* morpholinos (MO1: AGCCTGCATTATTTAGCCTTCTCTA (1.5 ng)
494 and MO2: GATGTCCTCTAAAAGAAAATGTCAG (0.75 ng)) were prepared as previously
495 reported and injected into *tg(kdrl:GFP)* embryos (Row et al., 2016). 2.5 ng of control
496 morpholino and *noto* morpholino were injected into *tg(kdrl:GFP)* embryos (Ouyang et al.,
497 2009).
498
499 **Microscopy and Imaging**
500 DIC and fluorescent time-lapse images of wild type, *noto* morphants, *aldh1a2* mutants,
501 and *tbx16* mutants were performed using a Leica DMI6000B inverted microscope with a
502 10× objective lens. Wild type and control embryos were siblings of the morphants and
503 mutants. Live embryos were mounted in 1% low-melt agarose in embryo media
504 containing 1x tricaine (25x stock 0.4g/l;Pentair,TRS1) in a 35mm glass bottom dish with
505 uncoated #1.5 coverslip and 20mm glass diameter (MatTek). In-situ hybridization
506 experiments were imaged using a M165FC microscope (Leica) equipped with an Infinity
507 3 camera (Lumenera). Embryos were mounted in either horizontal or flat mounted
508 configuration in 70% glycerol on glass slides.

509
510 Fluorescent images of trunk cross sections were imaged on a custom assembled
511 spinning disk confocal microscope consisting of an automated Zeiss frame, a Yokogawa
512 CSU-10 spinning disc, a Ludl stage controlled by a Ludl MAC6000 and an ASI filter
513 turret mated to a Photometrics Prime 95B camera. This microscope was controlled with
514 Metamorph microscope control software (V7.10.2.240 Molecular Devices), and laser
515 power levels were set in Vortran's Stradus VersaLase 8 software. Images were
516 processed in Fiji.
517
518 **Drug treatments**
519 RA was depleted in embryos using N,N-diethylaminobenzaldehyde (DEAB) and
520 BMS453. Stock concentrations of 20 mM DEAB in DMSO were diluted to working
521 concentrations of 20 μM in embryo media. Stock concentrations of 2 mM BMS453 in
522 DMSO were diluted to working concentrations of 2 μM in embryo media. Treatments
523 were done on shield stage embryos unless otherwise noted. All-trans RA was used to
524 activate the RA pathway. Stock concentrations of All-trans RA were diluted from 1 mM
525 stock to 0.1 μM working concentrations in embryo media. All treatments for all-trans RA
526 were performed in tailbud stage.
527
528 **Generation of explants for imaging**
529 Transgenic or mutant embryos were grown to the 10 somite stage and then transferred
530 to Modified Barth's Saline (MBS) (Sigma). In this medium, embryos were anesthetized
531 with 1 x Tricaine (25x stock 0.4g/l; Pentair, TRS1) and had their chorions manually
532 removed by forceps. The embryos were then sectioned with a 0.15mm microknife (Fine
533 Science Tools). Excess yolk was removed with the microknife, and the embryo was then
534 transferred to 35 mm glass-bottom dish (Matek) with a fire polished pipette. 1% low
535 gelling temperature agarose in MBS was heated to 40°C and placed over the embryo in
536 the proper orientation. The agarose was allowed to solidify and the explant was time-
537 lapsed using fluorescent and DIC microscopy.
538
539 **Quantification and Statistical Analysis**
540 When determining the fluorescence of angioblasts at the midline of the embryo, we
541 utilized the integrated density feature of Fiji software for image analysis. We calculated
542 the corrected total fluorescence of the area at the midline and of the whole embryo,

using the notochord as a reference for the midline. Corrected total fluorescence for the midline was calculated as: (mean gray value of midline x area of midline) - (mean gray value of background x area of midline). Corrected total fluorescence for the embryo was calculated: (mean gray value of embryo x area of embryo) - (mean gray value of background x area of embryo). Percentages for fluorescent intensity were calculated as (corrected total fluorescence at the midline) / (corrected total fluorescence of the whole embryo). Tracks for cells were made using the Trackmate plug-in for Fiji (Tinevez et al., 2017). We utilized a Laplacian of Gaussian detector and a Simple LAP Tracker to generate the tracks and analysis. P-values for indicated figures were generated using two-tailed unpaired student t-tests. Graphs were generated using Graphpad Prism 8.4.2 for dot plots, and Excel for line graphs. The black lines indicate the median and interquartile ranges, and were generated using the Prism software. Simple linear regression was also determined using Graphpad software.

Acknowledgments

We thank David Matus for critical review of the manuscript, as well as members of the Martin and Matus labs for helpful comments. We thank Jesus Torres Vazquez for sending the kdrl transgenic reporter lines. We thank Neal Bhattacharji and Stephanie Flanagan for excellent zebrafish care. We thank Tianying Chen for assistance in data acquisition. We thank Rebecca Adikes, Thom Geer and Nobska Imaging for microscopy support. This work was supported by the NSF (IOS 1452928) and NIH NIGMS (R01GM124282).

References

Amacher SL, Draper BW, Summers BR, Kimmel CB. 2002. The zebrafish T-box genes no tail and spadetail are required for development of trunk and tail mesoderm and medial floor plate. *Development* **129**:3311–3323.

Balmer S, Nowotschin S, Hadjantonakis AK. 2016. Notochord morphogenesis in mice: Current understanding and open questions. *Dev Dyn* **245**:547–557. doi:10.1002/dvdy.24392

Berenguer M, Lancman JJ, Cunningham TJ, Dong PDS, Duester G. 2018. Mouse but not zebrafish requires retinoic acid for control of neuromesodermal progenitors and body axis extension. *Dev Biol* **441**:127–131. doi:10.1016/j.ydbio.2018.06.019

577 Bernheim S, Meilhac SM. 2020. Mesoderm patterning by a dynamic gradient of retinoic
578 acid signalling: Retinoic acid patterning. *Philos Trans R Soc B Biol Sci* **375**:1809.
579 doi:10.1098/rstb.2019.0556rstb20190556
580 Blagden CS, Currie PD, Ingham PW, Hughes SM. 1997. Notochord induction of
581 zebrafish slow muscle mediated by sonic hedgehog. *Genes Dev*.
582 doi:10.1101/gad.11.17.2163
583 Casie Chetty S, Rost MS, Enriquez JR, Schumacher JA, Baltrunaite K, Rossi A, Stainier
584 DYR, Sumanas S. 2017. Vegf signaling promotes vascular endothelial
585 differentiation by modulating etv2 expression. *Dev Biol* **424**:147–161.
586 doi:10.1016/j.ydbio.2017.03.005
587 Chng SC, Ho L, Tian J, Reversade B. 2013. ELABELA: A hormone essential for heart
588 development signals via the apelin receptor. *Dev Cell* **27**:672–680.
589 doi:10.1016/j.devcel.2013.11.002
590 Cleaver O, Krieg P a. 1998. VEGF mediates angioblast migration during development of
591 the dorsal aorta in Xenopus. *Development* **125**:3905–14.
592 Drake CJ, Fleming PA. 2000. Vasculogenesis in the day 6.5 to 9.5 mouse embryo.
593 *Blood* **95**:1671–9. doi:10.1016/j.stem.2010.07.016
594 Duester G. 2008. Retinoic Acid Synthesis and Signaling during Early Organogenesis.
595 *Cell*. doi:10.1016/j.cell.2008.09.002
596 Emoto Y, Wada H, Okamoto H, Kudo A, Imai Y. 2005. Retinoic acid-metabolizing
597 enzyme Cyp26a1 is essential for determining territories of hindbrain and spinal cord
598 in zebrafish. *Dev Biol*. doi:10.1016/j.ydbio.2004.11.023
599 Fouquet B, Weinstein BM, Serluca FC, Fishman MC. 1997. Vessel patterning in the
600 embryo of the zebrafish: Guidance by notochord. *Dev Biol* **183**:37–48.
601 doi:10.1006/dbio.1996.8495
602 Freyer L, Hsu CW, Nowotschin S, Pauli A, Ishida J, Kuba K, Fukamizu A, Schier AF,
603 Hoodless PA, Dickinson ME, Hadjantonakis AK. 2017. Loss of Apela Peptide in
604 Mice Causes Low Penetrance Embryonic Lethality and Defects in Early
605 Mesodermal Derivatives. *Cell Rep* **20**:2116–2130. doi:10.1016/j.celrep.2017.08.014
606 Glickman NS, Kimmel CB, Jones MA, Adams RJ. 2003. Shaping the zebrafish
607 notochord. *Development* **130**:873–887. doi:10.1242/dev.00314
608 Goto H, Kimmey SC, Row RH, Matus DQ, Martin BL. 2017. FGF and canonical Wnt
609 signaling cooperate to induce paraxial mesoderm from tailbud neuromesodermal
610 progenitors through regulation of a two-step epithelial to mesenchymal transition.

611 *Development* **144**:1412–1424. doi:10.1242/dev.143578
612 Griffin KJ, Amacher SL, Kimmel CB, Kimelman D. 1998. Molecular identification of
613 spadetail: regulation of zebrafish trunk and tail mesoderm formation by T-box
614 genes. *Development* **125**:3379–3388.
615 Halpern ME, Thisse C, Ho RK, Thisse B, Riggleman B, Trevarrow B, Weinberg ES,
616 Postlethwait JH, Kimmel CB. 1995. Cell-autonomous shift from axial to paraxial
617 mesodermal development in zebrafish floating head mutants. *Development*
618 **121**:4257–4265. doi:10.1016/0168-9525(96)81431-4
619 Hamade A, Deries M, Begemann G, Bally-Cuif L, Genêt C, Sabatier F, Bonnieu A,
620 Cousin X. 2006. Retinoic acid activates myogenesis in vivo through Fgf8 signalling.
621 *Dev Biol* **289**:127–140. doi:10.1016/j.ydbio.2005.10.019
622 Heine UI, Roberts AB, Munoz EF, Roche NS, Sporn MB. 1986. Effects of retinoid
623 deficiency on the development of the heart and vascular system of the quail
624 embryo. *Virchows Arch B Cell Pathol Incl Mol Pathol*. doi:10.1007/BF02889897
625 Helker CSM, Schuermann A, Pollmann C, Chng SC, Kiefer F, Reversade B, Herzog W.
626 2015. The hormonal peptide Elabela guides angiob lasts to the midline during
627 vasculogenesis. *Elife* **4**:1–13. doi:10.7554/eLife.06726
628 Hinits Y, Osborn DPS, Hughes SM. 2009. Differential requirements for myogenic
629 regulatory factors distinguish medial and lateral somitic, cranial and fin muscle fibre
630 populations. *Development* **136**:403–414. doi:10.1242/dev.028019
631 Ho RK, Kane DA. 1990. Cell-autonomous action of zebrafish spt-1 mutation in specific
632 mesodermal precursors. *Nature*. doi:10.1038/348728a0
633 Hogan KA, Bautch VL. 2004. Blood Vessel Patterning at the Embryonic Midline. *Curr*
634 *Top Dev Biol* **62**:55–85.
635 Hollway GE, Bryson-Richardson RJ, Berger S, Cole NJ, Hall TE, Currie PD. 2007.
636 Whole-Somite Rotation Generates Muscle Progenitor Cell Compartments in the
637 Developing Zebrafish Embryo. *Dev Cell* **12**:201–219.
638 doi:10.1016/j.devcel.2007.01.001
639 Isogai S, Horiguchi M, Weinstein BM. 2001. The vascular anatomy of the developing
640 zebrafish: An atlas of embryonic and early larval development. *Dev Biol* **230**:278–
641 301. doi:10.1006/dbio.2000.9995
642 Janesick A, Nguyen TTL, Aisaki K -i., Igarashi K, Kitajima S, Chandraratna RAS, Kanno
643 J, Blumberg B. 2014. Active repression by RAR signaling is required for vertebrate
644 axial elongation. *Development* **141**:2260–2270. doi:10.1242/dev.103705

645 Janesick A, Tang W, Shioda T, Blumberg B. 2018. RARγ is required for mesodermal
646 gene expression prior to gastrulation in xenopus. *Dev* **145**:2–9.
647 doi:10.1242/dev.147769
648 Jin SW, Beis D, Mitchell T, Chen JN, Stainier DYR. 2005. Cellular and molecular
649 analyses of vascular tube and lumen formation in zebrafish. *Development*
650 **132**:5199–5209. doi:10.1242/dev.02087
651 Kimelman D. 2016. Tales of tails (and trunks): forming the posterior body in vertebrate
652 embryos David Kimelman. *Curr Top Dev Biol* **116**:517–536.
653 doi:10.1016/bs.ctdb.2015.12.008.Tales
654 Kimmel CB, Ballard WW, Kimmel SR, Ullmann B, Schilling TF. 1995. Stages of
655 embryonic development of the zebrafish. *Dev Dyn* **203**:253–310.
656 doi:10.1002/aja.1002030302
657 Kimmel CB, Kane DA, Walker C, Warga RM, Rothman MB. 1989. A mutation that
658 changes cell movement and cell fate in the zebrafish embryo. *Nature*.
659 doi:10.1038/337358a0
660 Kohli V, Schumacher JA, Desai SP, Rehn K, Sumanas S. 2013. Arterial and Venous
661 Progenitors of the Major Axial Vessels Originate at Distinct Locations. *Dev Cell*
662 **25**:196–206. doi:10.1016/j.devcel.2013.03.017
663 Kumar S, Duester G. 2014. Retinoic acid controls body axis extension by directly
664 repressing Fgf8 transcription. *Dev* **141**:2972–2977. doi:10.1242/dev.112367
665 Leal MA, Fickel SR, Sabillo A, Ramirez J, Vergara HM, Nave C, Saw D, Domingo CR.
666 2014. The Role of Sdf-1α signaling in Xenopus laevis somite morphogenesis. *Dev*
667 *Dyn*. doi:10.1002/dvdy.24092
668 Li J, Yue Y, Dong X, Jia W, Li K, Liang D, Dong Z, Wang X, Nan X, Zhang Q, Zhao Q.
669 2015. Zebrafish foxc1a plays a crucial role in early somitogenesis by restricting the
670 expression of aldh1a2 directly. *J Biol Chem* **290**:10216–10228.
671 doi:10.1074/jbc.M114.612572
672 Lohnes D, Mark M, Mendelsohn C, Dolle P, Dierich A, Gorry P, Gansmuller A, Chambon
673 P. 1994. Function of the retinoic acid receptors (RARs) during development. (I)
674 Craniofacial and skeletal abnormalities in RAR double mutants. *Development*
675 **120**:2723–2748.
676 Mandal A, Rydeen A, Anderson J, Sorrell MRJ, Zygmunt T, Torres-Vázquez J, Waxman
677 JS. 2013. Transgenic retinoic acid sensor lines in zebrafish indicate regions of
678 available embryonic retinoic acid. *Dev Dyn* **242**:989–1000. doi:10.1002/dvdy.23987

679 Manning AJ, Kimelman D. 2015. Tbx16 and Msgn1 are required to establish directional
680 cell migration of zebrafish mesodermal progenitors. *Dev Biol* **406**:172–185.
681 doi:10.1016/j.ydbio.2015.09.001
682 Martin BL. 2016. Factors that coordinate mesoderm specification from neuromesodermal
683 progenitors with segmentation during vertebrate axial extension. *Semin Cell Dev*
684 *Biol* **49**:59–67. doi:10.1016/j.semcdb.2015.11.014
685 Martin BL, Kimelman D. 2012. Canonical Wnt Signaling Dynamically Controls Multiple
686 Stem Cell Fate Decisions during Vertebrate Body Formation. *Dev Cell* **22**:223–232.
687 doi:10.1016/j.devcel.2011.11.001
688 McMillen P, Holley SA. 2015. The tissue mechanics of vertebrate body elongation and
689 segmentation. *Curr Opin Genet Dev*. doi:10.1016/j.gde.2015.02.005
690 Mendelsohn C, Lohnes D, Decimo D, Lufkin T, LeMeur M, Chambon P, Mark M. 1994.
691 Function of the retinoic acid receptors (RARs) during development. (II) Multiple
692 abnormalities at various stages of organogenesis in RAR double mutants.
693 *Development* **120**:2749–2771.
694 Morgan CA, Parajuli B, Buchman CD, Dria K, Hurley TD. 2015. N,N-
695 diethylaminobenzaldehyde (DEAB) as a substrate and mechanism-based inhibitor
696 for human ALDH isoenzymes. *Chem Biol Interact* **234**:18–28.
697 doi:10.1016/j.cbi.2014.12.008
698 Niederreither K, Vermot J, Messaddeq N, Schuhbaur B, Chambon P, Dollé P. 2001.
699 Embryonic retinoic acid synthesis is essential for heart morphogenesis in the
700 mouse. *Development* **128**:1019–1031.
701 Norris ML, Pauli A, Gagnon JA, Lord ND, Rogers KW, Mosimann C, Zon LI, Schier AF.
702 2017. Toddler signaling regulates mesodermal cell migration downstream of nodal
703 signaling. *Elife* **6**:e22626. doi:10.7554/eLife.22626
704 Ouyang X, Shestopalov IA, Sinha S, Zheng G, Pitt CLW, Li WH, Olson AJ, Chen JK.
705 2009. Versatile synthesis and rational design of caged morpholinos. *J Am Chem*
706 *Soc* **131**:13255–13269. doi:10.1021/ja809933h
707 Pardanaud L, Altmann C, Kitos P, Dieterlen-Lievre F, Buck CA. 1987. Vasculogenesis in
708 the early quail blastodisc as studied with a monoclonal antibody recognizing
709 endothelial cells. *Development* **100**:339–349.
710 Pardanaud L, Luton D, Prigent M, Bourcheix LM, Catala M, Dieterlen-Lièvre F. 1996.
711 Two distinct endothelial lineages in ontogeny, one of them related to hemopoiesis.
712 *Development* **122**:1363–1371.

713 Pauli A, Norris ML, Valen E, Chew GL, Gagnon JA, Zimmerman S, Mitchell A, Ma J,
714 Dubrulle J, Reyon D, Tsai SQ, Joung JK, Saghatelian A, Schier AF. 2014. Toddler:
715 An embryonic signal that promotes cell movement via apelin receptors. *Science*
716 *(80-)* **343**. doi:10.1126/science.1248636
717 Pillay LM, Mackowetzky KJ, Widen SA, Waskiewicz AJ. 2016. Somite-derived retinoic
718 acid regulates zebrafish hematopoietic stem cell formation. *PLoS One*.
719 doi:10.1371/journal.pone.0166040
720 Row RH, Maître JL, Martin BL, Stockinger P, Heisenberg CP, Kimelman D. 2011.
721 Completion of the epithelial to mesenchymal transition in zebrafish mesoderm
722 requires Spadetail. *Dev Biol* **354**:102–110. doi:10.1016/j.ydbio.2011.03.025
723 Row RH, Pegg A, Kinney B, Farr GH, Maves L, Lowell S, Wilson V, Martin BL. 2018.
724 BMP and FGF signaling interact to pattern mesoderm by controlling basic helix-
725 loop-helix transcription factor activity. *Elife* **7**:e31018. doi:10.7554/eLife.31018
726 Row RH, Tsotras SR, Goto H, Martin BL. 2016. The zebrafish tailbud contains two
727 independent populations of midline progenitor cells that maintain long-term germ
728 layer plasticity and differentiate in response to local signaling cues. *Dev*.
729 doi:10.1242/dev.129015
730 Sandell LL, Sanderson BW, Moiseyev G, Johnson T, Mushegian A, Young K, Rey JP,
731 Ma JX, Staehling-Hampton K, Trainor PA. 2007. RDH10 is essential for synthesis of
732 embryonic retinoic acid and is required for limb, craniofacial, and organ
733 development. *Genes Dev* **21**:1113–1124. doi:10.1101/gad.1533407
734 Skvarca LB, Han HI, Espiritu EB, Missinato MA, Rochon ER, McDaniels MD, Bais AS,
735 Roman BL, Waxman JS, Watkins SC, Davidson AJ, Tsang M, Hukriede NA. 2019.
736 Enhancing regeneration after acute kidney injury by promoting cellular
737 dedifferentiation in zebrafish. *DMM Dis Model Mech*. doi:10.1242/dmm.037390
738 Sumanas S, Jorniak T, Lin S. 2005. Identification of novel vascular endothelial-specific
739 genes by the microarray analysis of the zebrafish cloche mutants. *Blood* **106**:534–
740 541. doi:10.1182/blood-2004-12-4653
741 Sumoy L, Bennett Keasey J, Dittman TD, Kimelman D. 1997. A role for notochord in
742 axial vascular development revealed by analysis of phenotype and the expression
743 of VEGR-2 in zebrafish flh and ntl mutant embryos. *Mech Dev* **63**:15–27.
744 doi:10.1016/S0925-4773(97)00671-0
745 Talbot WS, Trevarrow B, Halpern ME, Melby AE, Farr G, Postlethwait JH, Jowett T,
746 Kimmel CB, Kimelman D. 1995. A homeobox gene essential for zebrafish

747 notochord development. *Nature* **378**:150–157. doi:10.1038/378150a0
748 Tani S, Chung U il, Ohba S, Hojo H. 2020. Understanding paraxial mesoderm
749 development and sclerotome specification for skeletal repair. *Exp Mol Med*
750 **52**:1166–1177. doi:10.1038/s12276-020-0482-1
751 Tinevez JY, Perry N, Schindelin J, Hoopes GM, Reynolds GD, Laplantine E, Bednarek
752 SY, Shorte SL, Eliceiri KW. 2017. TrackMate: An open and extensible platform for
753 single-particle tracking. *Methods* **115**:80–90. doi:10.1016/j.ymeth.2016.09.016
754 Tlili S, Yin J, Rupprecht JF, Mendieta-Serrano MA, Weissbart G, Verma N, Teng X,
755 Toyama Y, Prost J, Saunders TE. 2019. Shaping the zebrafish myotome by
756 intertissue friction and active stress. *Proc Natl Acad Sci U S A* **116**:25430–25439.
757 doi:10.1073/pnas.1900819116
758 Yabe T, Takada S. 2016. Molecular mechanism for cyclic generation of somites:
759 Lessons from mice and zebrafish. *Dev Growth Differ* 31–42. doi:10.1111/dgd.12249
760 Yin C, Solnica-Krezel L. 2007. Convergence and extension movements affect dynamic
761 notochord-somite interactions essential for zebrafish slow muscle morphogenesis.
762 *Dev Dyn* **236**:2742–2756. doi:10.1002/dvdy.21295
763 Yin J, Lee R, Ono Y, Ingham PW, Saunders TE. 2018. Spatiotemporal Coordination of
764 FGF and Shh Signaling Underlies the Specification of Myoblasts in the Zebrafish
765 Embryo. *Dev Cell* **46**:735-750.e4. doi:10.1016/j.devcel.2018.08.024
766 Youn BW, Malacinski GM. 1981. Somitogenesis in the amphibian Xenopus laevis:
767 scanning electron microscopic analysis of intrasomitic cellular arrangements during
768 somite rotation. *J Embryol Exp Morphol* **64**:23–43.
769
770 **Supplemental Figures**

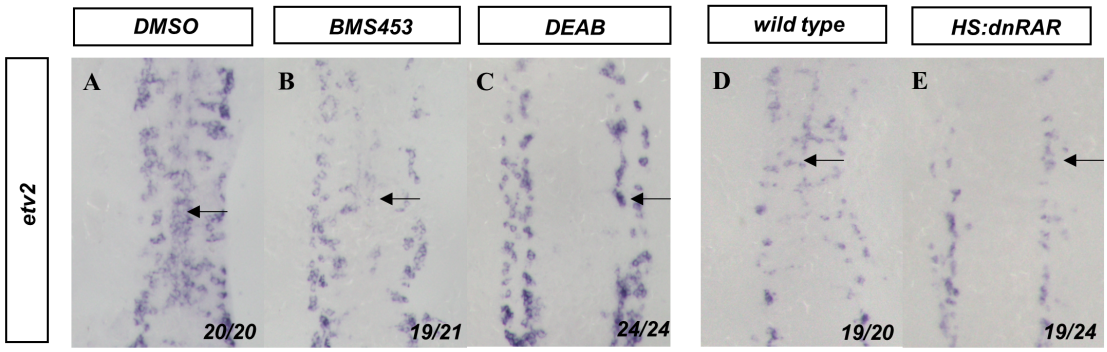

771

Figure S1. Three alternative methods of RA signaling disruption inhibit midline angioblast migration.
Angioblasts are labelled by *etv2* in-situ hybridization in 13-somite stage embryos (black arrows) after (**A**) DMSO, (**B**) BMS453, or (**C**) DEAB treatment, or after bud stage heat-shock in (**D**) wild type and (**E**) *HS:dnrar* embryos. Embryos are shown from a dorsal view with anterior to the top.

772

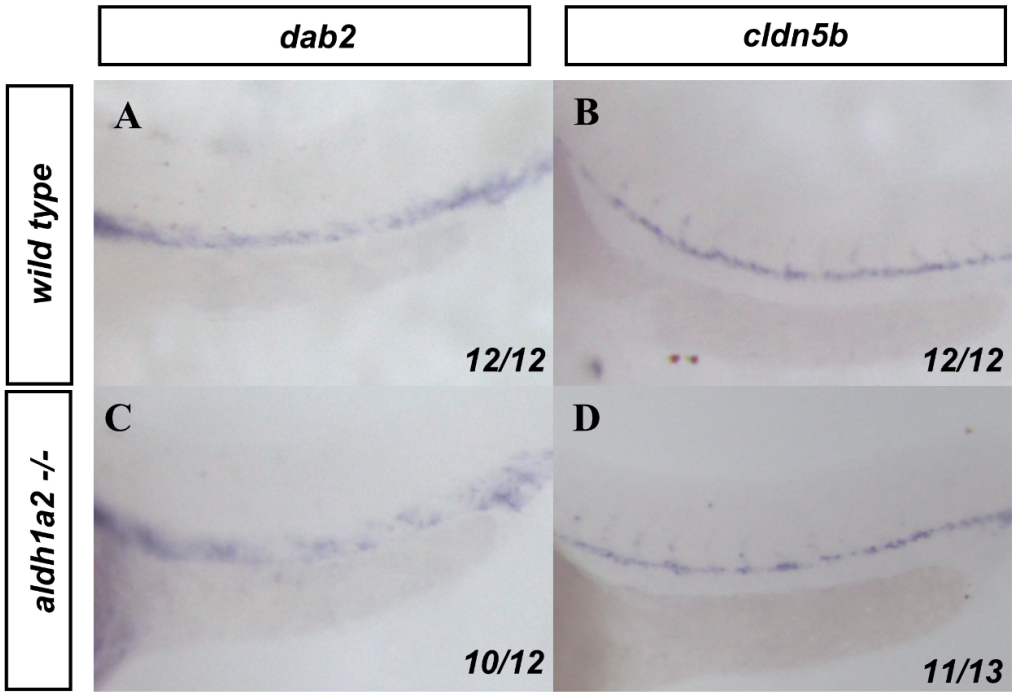

773

Figure S2. Effects of RA depletion on arterial and venous markers.
(A, C) *dab2* and (B, D) *cldn5b* in-situ hybridization labels the veins and arteries, respectively in (**A-B**) wild type or (**C-D**) aldh1a2 -/- embryos. Embryos are shown from a lateral view with anterior to the left.

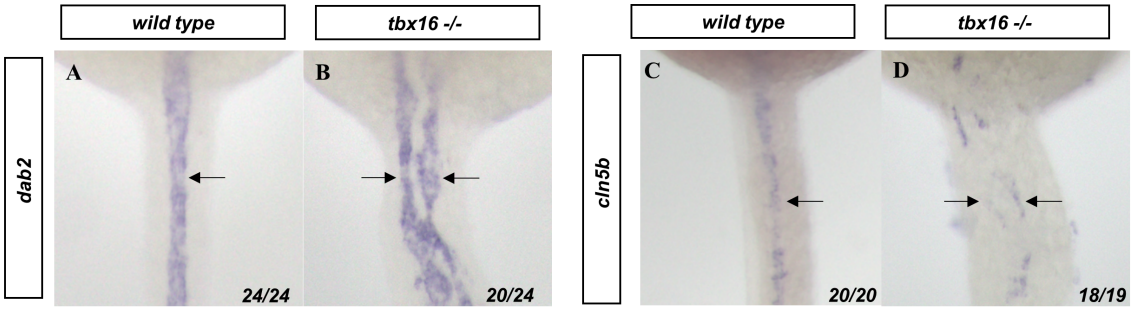

Figure S3. Bifurcated angioblasts in *tbx16* mutants preferentially join the venous population. (A, B) *dab2* and (C, D) *cldn5b* in-situ hybridization labels the veins and arteries, respectively (black arrows) in (**A,C**) wild type and (**B,D**) *tbx16* -/- embryos. Embryos are shown from a dorsal view with anterior to the top.

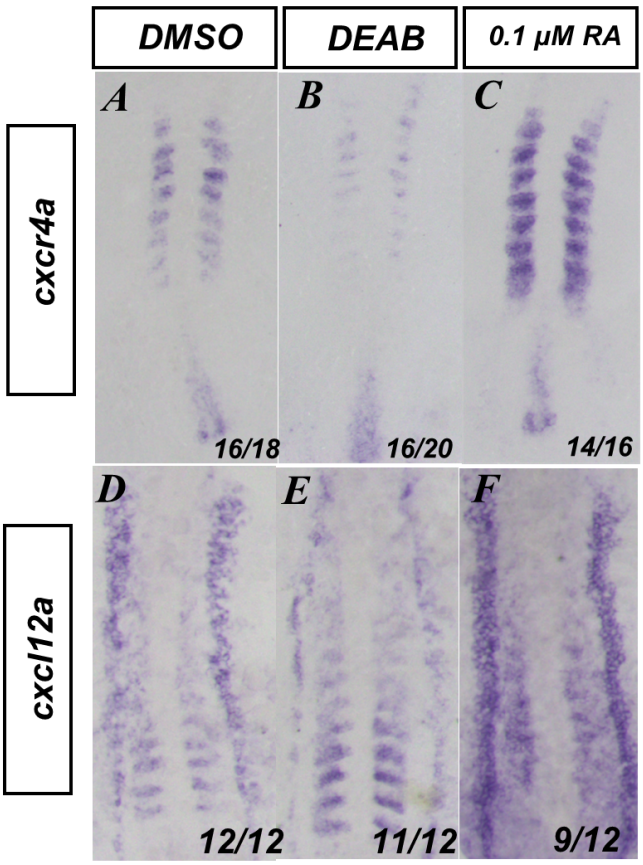

Figure S4. Retinoic acid signaling affects the expression of genes associated with somitic movements.
(**A-C**) In-situ hybridization for *cxcr4a and* (**D-F**) *cxcl12a* in (**A, D**) DMSO, (**B, E**) 20 μM DEAB, or (**C, F**) 0.1 μM RA treated embryos. Embryos are shown from a dorsal view with anterior to the top.

Movie S1. Time-lapse fluorescent imaging of *tg(kdrl:eGFP)* embryo at the 10 somite-stage. *tg(kdrl:eGFP)* marks angioblasts as they migrate to the midline. Angioblasts display the anterior posterior processivity while coalescing at the midline. Frame rate= one image/5 min. Run time= 235 min.

Movie S2. Time-lapse fluorescent imaging of *tg(kdrl:eGFP), aldh1a2 -/-* embryo at the 10 somite-stage. *tg(kdrl:eGFP)* marks angioblasts as they migrate to the midline. Angioblasts lose anterior to posterior processivity and show disrupted migration. Frame rate= one image/5 min. Run time= 235 min.

789

790 **Movie S3. Time-lapse fluorescent imaging of a 10 somite-stage**
791 ***tg(kdrl:eGFP)* embryo with addition of 0.1 μM RA at the tailbud stage.** *tg(kdrl:eGFP)*
792 marks angioblasts as they migrate to the midline. Angioblasts accelerate their
793 processivity towards the midline. Frame rate= one image/5 min. Run time= 235 min.
794

795 **Movie S4. Time-lapse fluorescent imaging of *HS:id3, HS;dnRAR* cells in a**
796 ***tg(kdrl:eGFP)* host.** Cells expressing *HS:id3, HS;dnRAR* migrate to the midline along
797 with angioblasts in a *tg(kdrl:eGFP)* host. Cells with dnRAR migrate faithfully with
798 angioblasts. Frame rate= one image/5 min. Run time= 180 min.
799

800 **Movie S5. Time-lapse fluorescent imaging of *tg(tbxta:kaede), tg(actc1b:gfp)***
801 **embryo trunks.** *tg(tbxta:kaede)* and *tg(actc1b:gfp)* label the notochord and somites,
802 respectively. The notochord displaces dorsally with respect to the ventral-most portion of
803 somites. Frame rate= one image/10 min. Run time= 290 min.
804

805 **Movie S6. Time-lapse fluorescent imaging of *tg(tbxta:kaede), tg(actc1b:gfp)***
806 **embryo trunks in 20 μM DEAB.** *tg(tbxta:kaede)* and *tg(actc1b:gfp)* label the notochord
807 and somites, respectively. In the absence of RA synthesis the notochord fails to displace
808 relative to the ventral-most portion of somites. Frame rate= one image/15 min. Run
809 time= 285 min.
810

811 **Movie S7. Time-lapse fluorescent imaging of *tg(tbxta:kaede), tg(actc1b:gfp)***
812 **embryo trunks in 0.1 μM RA .** *tg(tbxta:kaede)* and *tg(actc1b:gfp)* label the notochord
813 and somites, respectively. Addition of RA results in the notochord displacing early
814 relative to the ventral-most portion of the somites. Frame rate= one image/10 min. Run
815 time= 290 min.
816

817 **Movie S8. Time-lapse fluorescent imaging of *tg(tbxta:kaedae), tg(actc1b:gfp)* trunk**
818 **explant.** Trunk explant shows notochord displacement away from ventral-most portion of
819 somites. Frame rate= one image/15 min. Run time= 285 min.
820

821 **Movie S9. Time-lapse fluorescent and DIC imaging of *tg(kdrl:eGFP)* explant at the**
822 **10 somite-stage.** *tg(kdrl:eGFP)* marks angioblasts as they migrate to the midline. A

trunk explant, imaged around the 4th somite, shows normal migration of the angioblasts to the midline. Frame rate= one image/5 min. Run time= 85 min.

Movie S10. Time-lapse fluorescent and DIC imaging of *tg(kdrl:eGFP), aldh1a2 -/-* explant at the 10 somite-stage. *tg(kdrl:eGFP)* marks angioblasts as they migrate to the midline. A trunk explant with mutant *aldh1a2* shows no angioblast migration and no notochord displacement. Frame rate= one image/5 min. Run time= 85 min.

Movie S11. Time-lapse confocal fluorescent imaging of a *HS:mcherry-caax-p2a-NLS-kikume* embryo in DMSO treatment. *HS:mcherry-caax-p2a-NLS-kikume* marks nuclei within the somite. Sample tracks ranging from red (most displacement) to blue (least displacement) show broad movement within the somite. Frame rate= one image/5 min. Run time= 240 min.

Movie S12. Time-lapse confocal fluorescent imaging of a *HS:mcherry-caax*-*p2a-NLS-kikume* embryo in DEAB treatment. *HS:mcherry-caax-p2a-NLS-kikume* marks nuclei within the somite. Sample tracks ranging from red (most displacement) to blue (least displacement) show little directional movement in 20 μM DEAB treatment conditions. Frame rate= one image/5 min. Run time= 240 min.